Suspended Si ring resonator for mid-IR application

Yang Xia, Ciyuan Qiu, Xuezhi Zhang, Weilu Gao, Jie Shu, and Qianfan Xu*

Department of Electrical and Computer Engineering, Rice University, Houston, Texas 77005, USA
**Corresponding author: qianfan@rice.edu*

Received January 21, 2013; accepted February 12, 2013;
posted February 28, 2013 (Doc. ID 183815); published March 26, 2013

In this Letter we fabricate and characterize suspended silicon (Si) waveguides and ring resonators for mid-infrared wavelength range. Both tunable laser and thermal tuning are used to cover wavelength ranges near 5.2 and 3.4 μm. The loaded quality factors are estimated at 2700 at 5.2 μm and 7900 at 3.4 μm. Heat induced spectrum distortion is observed. Absorption loss is analyzed based on the spectrum distortion, simulation, and all-optical modulation. It is shown that main loss comes from scattering at surface and should be possible to reduce by improving fabrication process.

OCIS codes: 130.3060, 130.3120, 130.3990.

Mid-infrared (MIR) wavelength range plays an important role in sensing and analyzing a variety of materials, since many molecules important to our life have vibration modes with frequency fingerprint in this range [1,2]. Conventional photonic structures fabricated on silicon-on-insulator (SOI) wafer don't work well for MIR wavelengths longer than 4 μm due to the material absorption in SiO_2. To overcome this limitation, waveguides on silicon-on-sapphire (SOS) substrates have been demonstrated [3,4]. But this approach depends on the SOS wafer that is more expensive and less commonly used. Another way to avoid the absorption loss in SiO_2 at MIR is to etch away the oxide under-cladding layer to form a suspended structure [5–7].

In this Letter, we demonstrate suspended silicon ring resonators operating near the MIR wavelengths of 5.2 and 3.39 μm. We show the loaded quality factor can be ~2700 and ~7900 for those two wavelengths, respectively. We also study the spectrum distortion at high-input power and all-optical modulation, determine the proportion of absorption taking in total loss and conclude the absorption is not the main loss factor.

The devices are fabricated on an SOI wafer with 750 nm thick Si on top and 3 μm thick SiO_2 under it. To suspend the waveguide we adopt a ridge waveguide structure. The width and height of the ridge waveguide are designed at 1.6 μm and 500 nm, while the thickness of the slab is 250 nm, which is close to the largest dimension for a single mode waveguide at the wavelength of 5.2 μm. Holes are open on the slab so that buffered oxide etch (BOE) can reach the SiO_2 layer under the slab and etch it locally to suspend the ridge waveguide, as shown in Fig. 1(a). Each device contains seven ring resonators side coupled to a U-shape waveguide, whose input and output terminate at the same edge of the chip. The diameters of the rings in each device vary slightly around 35 μm, so that their resonant wavelengths are expected to space evenly in a free-spectral range (FSR) (i.e., the resonances of neighboring rings differ by FSR/7). The rings along each waveguide have the same coupling gaps between the waveguide and the ring. Multiple waveguides with different gap sizes are used to obtain critical coupling at different wavelengths. The coupling between the device and the input/output free space waves is realized by taper waveguide at the edge of the chip with tip width of 700 nm. The edge-to-edge distance between the waveguide and the hole is 2.5 μm except for the coupling areas, where one or two holes slightly deviate from this distance for one of the two closely placed waveguides. According to simulation, the field within 1.5 μm around the ridge contains more than 99.9% of the total power, so that the turbulence of the holes is negligible, except for the taper area where waveguide is narrower and mode distribution is wider.

The fabrication process starts from thickening the silicon layer on an SOI wafer from 250 to 750 nm using epitaxial growth. Then the device is fabricated using two-stage electron beam lithography (EBL) and reactive ion etching (RIE) process. In the first stage, the ridge is patterned on the SOI wafer by EBL with negative resist XR 1541 followed by an RIE process. The thin Si slab is left whose thickness is controlled by the RIE time. Next, another EBL is taken to define the pattern of the holes with PMMA as positive resist on the slab, and the holes are etched open by RIE. Then the wafer is immersed into BOE so that the SiO_2 underneath is removed by wet etching. The SEM picture of the fabricated device is shown in Fig. 1(b). The width of the waveguide is measured to be ~1.5 μm.

Two continuous-wave MIR lasers are used to characterize the ring resonator, a fix-wavelength He–Ne gas laser at the wavelength of 3.39 μm and a tunable quantum–cascade laser with mode-hopping-free tuning range from 5.116 to 5.221 μm. Both lasers are adjusted to be TE polarized. A PbSe-based IR detector is used to measure the output power from the device. Since the detector can only detect AC signals, an optical chopper is used to modulate the laser light in low frequency, and the signal

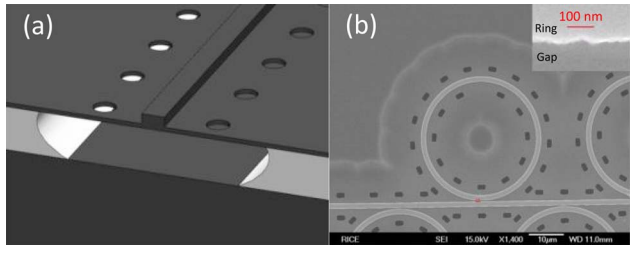

Fig. 1. (Color online) (a) Designed suspended MIR waveguide structure. (b) SEM picture of the fabricated device. The inset is a top-view SEM picture of the coupling gap between the ring and the straight waveguide.

from the photodetector is phase-locked with the modulation signal using a lock-in amplifier. This way, only the signal at the modulation frequency is picked and amplified, and the noise in other frequency range is filtered. A typical transmission spectrum at around 5.2 μm is measured with the tunable laser and shown as the green squares in Fig. 2. The spectral is fitted with the theoretical transmission spectrum of ring resonators

$$\text{Tran} = 1 - \frac{(1 - e^{-2\gamma})(1 - t^2)}{(1 - te^{-\gamma})^2 + 4te^{-\gamma}\sin^2\left(\frac{\phi}{2}\right)}, \tag{1}$$

$$\phi = \frac{2\pi^2 D}{\lambda}\left[n_{\text{eff}} + \frac{\partial n_{\text{eff}}}{\partial \lambda}(\lambda - \lambda_0)\right], \tag{2}$$

where γ is the intrinsic loss efficient in the cavity, t is the transmission efficient of the coupling between the resonator and the bus waveguide, D is the diameter of the ring and n_{eff} is the effective index of the waveguide mode that is obtained by a mode solver in COMSOL. From the fitting, the intrinsic Q of the resonator is ~6800, corresponding to a waveguide loss of ~31 dB/cm.

We use a fix-wavelength He–Ne laser to characterize the spectral property of the resonator at the wavelength of 3.39 μm, which is done by a thermal tuning method [8]. A thermal–electrical cooler is used to control the temperature of the chip. When the temperature changes, the refractive index of silicon at the wavelength of 3.39 μm changes with a rate of 1.7×10^{-4} K^{-1} [9]. As the result, the effective index of the resonant mode changes at a rate of 1.8×10^{-4} K^{-1}. The change of the refractive index of silicon modifies the mode distribution, so that the change in effective index becomes larger than the change in the refractive index of silicon [8]. The change in effective index causes a change in optical transmission following Eq. (1) and

$$\phi = \frac{2\pi^2 D}{\lambda}\left[n_{\text{eff}} + \frac{\partial n_{\text{eff}}}{\partial T}(T - T_0)\right]. \tag{3}$$

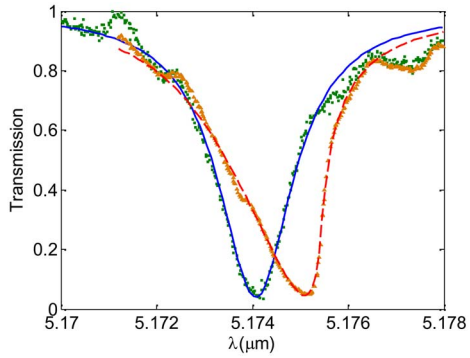

Fig. 2. (Color online) Normalized transmission spectra of the ring resonator with a waveguide-to-ring gap of ~900 nm. The green squares and the blue solid line: measured and fitted spectra with an input optical power of 0.035 mW. The orange triangles and the red dashed line: measured and fitted spectra with an input optical power of 1.46 mW.

The measured transmission versus temperature relationship is shown as the green dots in Fig. 3, which is fitted by the blue line, which is calculated from Eqs. (1) and (3). From the fitting, the intrinsic Q of the resonator at this wavelength is calculated to be ~11000, which corresponds to a waveguide loss of ~27 dB/cm [8]. The loss at this wavelength is just slightly lower than that at 5.2 μm, which is mainly due to higher mode confinement at shorter wavelengths.

The waveguide loss mainly consists of scattering loss from surface roughness and absorption loss from surface states [10]. Since the absorbed optical energy is eventually converted to heat, we can estimate the absorption loss from the temperature change of the device. When the input optical power is high, the optical absorption in the ring can cause enough heating that causes measurable change in the optical transmission. As the result, the measured transmission spectrum has an unsymmetrical shape [11] as shown by the orange triangles in Fig. 2. At the input power of 1.46 mW, the resonance shifts by ~1.2 nm, which corresponds to a change in n_{eff} of $\sim 5.5 \times 10^{-4}$. While index change can also be caused by the Kerr effect, that effect is negligibly small at this input power. The index change from the Kerr effect is estimated to be on the order of 10^{-7}.

To account for the absorption-induced temperature change, Eq. (2) is updated as

$$\phi = \frac{2\pi^2 D}{\lambda}\left[n_{\text{eff}} + \frac{\partial n_{\text{eff}}}{\partial \lambda}(\lambda - \lambda_0) + \frac{\partial n_{\text{eff}}}{\partial T}\frac{\eta P_A(1 - \text{Tran})}{K}\right]. \tag{4}$$

Here K denotes the average temperature change in the resonator with unit heating power, which is obtained by thermal simulation using the software COMSOL. P_A is the power input to the resonator and η is ratio between the absorption loss and total loss. By fitting the measured spectral with Eqs. (1) and (4), which is shown as the red dashed line in Fig. 2, η is found to be ~0.21. Therefore, optical absorption accounts for a small portion of the waveguide loss at ~6.5 dB/cm, while scattering accounts for the rest.

Absorption-induced temperature change allows us to perform all-optical thermo-optic switching at the MIR wavelengths. The experimental setup is shown in

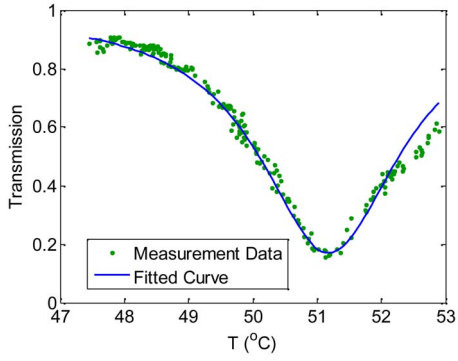

Fig. 3. (Color online) Spectrum near 3.39 μm measured by thermal tuning. Measured on a device with a waveguide-to-ring gap of ~360 nm.

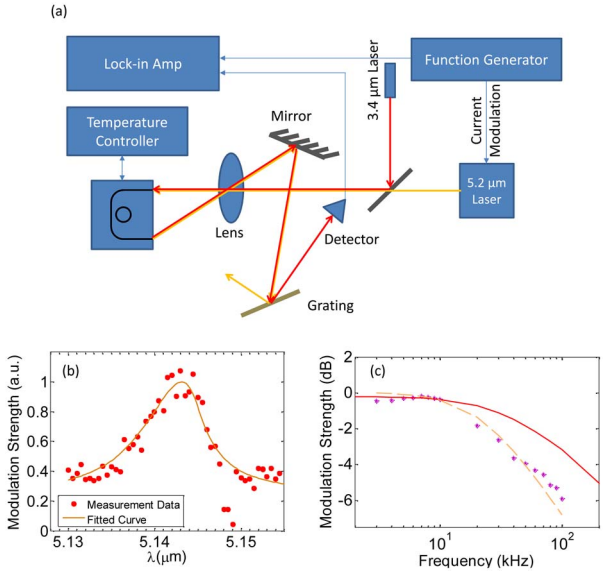

Fig. 4. (Color online) (a) Optical modulation measurement setup. (b) Optical modulation response with respect to pump wavelength. (c) Frequency response for optical modulation and fitting curve (the purple stars: experimental result; the orange dashed line: fitting curve; the red solid line: simulation result).

Fig. 4(a). The tunable laser at 5.2 μm is used as pump, which is coupled into one end of the U-shaped waveguide along with the probe laser at 3.39 μm. The optical outputs from the waveguide is collimated and separated from the input with a mirror [12]. A grating is used to separate the pump and probe components and the probe light is sent to the photodetector. The pump light is modulated at frequency f by changing the pump current, and the f-component of the modulation on the probed light is obtained from the detector and a lock-in amplifier. The temperature of the chip is adjusted to 50°C in order to maximize the modulation depth, which happens when the probe light aligns with the part of spectrum (see Fig. 3) with the steepest slope.

Figure 4(b) shows intensity of the modulated optical output at 3.39 μm when the wavelength of the pump laser is tuned. As expected, the modulation strength M is maximized when the pump laser aligns with the ring resonance, so that more power is coupled into the ring. Since the device has a smaller coupling gap of 360 nm between the waveguide and the resonator, the quality factor for the 5.2 μm band decreases significantly, resulting in the broader resonance bandwidth and lower resonant enhancement. The modulation depth is proportional to the intensity of light in the ring resonator and in the waveguide adjacent to the ring. The measured wavelength dependency is fitted to the theory (solid line in Fig. 4(a), which gives an intrinsic Q of ~6400 at the pump wavelength. This Q corresponds to a loss of 32 dB/cm, which is close to the loss in the device shown in Fig. 2.

To measure the bandwidth of this modulation and characterize the thermal response time, we show in Fig. 4(c) how the modulation strength changes with the frequency f. The measured data is fitted with a low-pass filter model (orange dashed line) and a time constant of $\tau = 7.5$ μs is obtained. The relatively long response time confirms our assumption that the modulation is induced by slow process such as thermal effect. We simulate the thermal response of the suspended silicon ridge-ring structure using COMSOL and the result is plotted as the red solid line in Fig. 4(c). The slightly higher bandwidth in the simulation may be due to neglecting the contribution from the bus waveguide near the ring, which slows the system response by increasing its heat capacitance.

In summary, we designed and fabricated suspended silicon ring resonators and demonstrated their operation at MIR wavelengths. The devices show intrinsic quality factors of ~6800 at 5.2 μm wavelength band and ~11000 at 3.39 μm wavelength band. We found that optical absorption accounts for ~21% of the total waveguide loss while optical scattering accounts for the rest. We expect the optical loss can be improved by optimizing fabrication process and applying certain post processes, such as piranha washing [3] and oxidation smoothing [13].

References

1. K. Miyamoto, K. Ishibashi, K. Hiroi, Y. Kimura, H. Ishii, and M. Niwano, Appl. Phys. Lett. **86**, 053902 (2005).
2. F. K. Tittel, Y. Bakhirkin, A. Kosterev, R. Lewicki, S. So, G. Wysocki, and R. F. Curl, Proc. SPIE **6900**, 69000Z (2008).
3. T. Baehr-Jones, A. Spott, R. Ilic, A. Spott, B. Penkov, W. Asher, and M. Hochberg, Opt. Express **18**, 12127 (2010).
4. A. Spott, Y. Liu, T. Baehr-Jones, R. Ilic, and M. Hochberg, Appl. Phys. Lett. **97**, 213501 (2010).
5. R. Soref, Nat. Photonics **4**, 495 (2010).
6. Z. Cheng, X. Chen, C. Y. Wong, K. Xu, C. K. Y. Fung, Y. M. Chen, and H. K. Tsang, Opt. Lett. **37**, 1217 (2012).
7. Z. Cheng, X. Chen, C. Y. Wong, K. Xu, and H. K. Tsang, IEEE Photon. J. **4**, 1510 (2012).
8. C. Y. Wong, Z. Cheng, X. Chen, K. Xu, C. K. Y. Fung, Y. M. Chen, and H. K. Tsang, IEEE Photon. J. **4**, 1095 (2012).
9. B. J. Frey, D. B. Leviton, and T. J. Madison, Proc. SPIE **6273**, 62732J (2006).
10. T. Baehr-Jones, M. Hochberg, and A. Scherer, Opt. Express **16**, 1659 (2008).
11. Q. Xu and M. Lipson, Opt. Lett. **31**, 341 (2006).
12. Q. Xu, D. Fattal, and R. G. Beausoleil, Opt. Express **16**, 4309 (2008).
13. D. K. Sparacin, S. J. Spector, and L. C. Kimerling, J. Lightwave Technol. **23**, 2455 (2005).